EUROPEAN WORKSHOP ON ON-BOARD DATA PROCESSING (OBDP2021), 14-17 JUNE 2021

HYPERSPECTRAL DIGITAL BACKEND BREADBOARDING FOR MICROWAVE RADIOMETERS. 183 GHZ WATER VAPOUR ABSORPTION BAND APPLICATION TO SAPHIR-NG SENSOR

MÈGE, Alexandre [(1)], CARAYON, Benjamin [(2)], GONZALEZ, Patrice [(3)], JEANNIN, Nicolas [(4)], PUECH, Jérôme [(5)]

[(1)] Airbus Defence and Space, Elancourt, 1 boulevard Jean Moulin,CS 30503 France - 78990 Elancourt Cedex, Email: alexandre.mege@airbus.com

[(2)] Airbus Defence and Space, Toulouse, 31 rue des Cosmonautes, 31400 Toulouse, Email: benjamin.b.carayon@airbus.com

[(3)] Service Instrumentation Radar et Performances – CNES - 18 avenue Edouard Belin 31401 Toulouse Cedex 9, Email: patrice.gonzalez@cnes.fr

[(4)] Airbus Defence and Space, Toulouse, 31 rue des Cosmonautes, 31400 Toulouse, Email: nicolas.jeannin@airbus.com

[(5)] Service Instrumentation Radar et Performances – CNES - 18 avenue Edouard Belin 31401 Toulouse Cedex 9, Email: Jerome.Puech@cnes.fr

ABSTRACT

In order to improve meteorological models, measurement of the atmospheric profile for water vapour is an important parameter. Space based radiometers measuring the H_2O absorption band at 183 GHz can be used to measure this atmospheric profile.

SAPHIR is a radiometer instrument aboard the Megha-Tropiques spacecraft measuring the H_2O absorption band at 183 GHz using 6 sub-bands from 200 to 2000 MHz. For SAPHIR-NG, a hyperspectral radiometer is considered in order to measure the absorption band using at least 256 channels over more than 10 GHz. Standard solutions based on analog filters are not viable in such a configuration, so a digital solution is required.

This CNES R&T study aims at developing a demonstrator of the digital backend of this hyperspectral radiometer based on FPGA and high speed ADC. Based on a previous study, an optimum is proposed for 256 channels over 10 GHz of bandwidth with a quantization between 4 to 6 bits at the ADC output.

The on-board digital signal processing is a filter bank followed by a power detector. A simulation of the impact of the FIR filter length and the filter window shape (rectangular, Hamming, Blackman ...) on the measurement quality (radiometric sensitivity) is performed.

The filter bank implementation in FPGA and ASIC is based on the optimised polyphase filter architecture, using a Fast Fourier Transform to efficiently channelize the signal.

In the frame of the demonstrator architecture definition, detailed trade-off between commercial and radiation tolerant FPGAs (Zynq Ultrascale+ RFSOC, Space Grade Kintex ultrascale, Versal AI Core and NG-ULTRA) and giga-sample ADC (EV12AQ600, ADC12DJ3200QML and ADC12DJ5200RF) are performed to select best candidates for the demonstrator.

In parallel of the FPGA based demonstrator, study of an ASIC based solution is ongoing in order to reduce the estimated 10 W consumption for the 10 GHz bandwidth acquisition and processing FPGA based solution to approximately 3 W.

1. Absorption radiometry

Earth brightness temperature in the RF spectrum is linked to the atmospheric profile.
The H_2O absorption band at 183 GHz is of particular interest for meteorological applications to measure the atmospheric humidity and temperature profile.
A specific temperature and humidity atmospheric profile will result in a specific brightness spectrum profile in the H_20 band at 183 GHz. Examples of atmospheric profiles and of the corresponding brightness temperatures are illustrated in *Figure 1* and in *Figure 2* respectively.
By measuring the brightness spectrum and inverting the process, an atmospheric profile for humidity and temperature can be recovered.

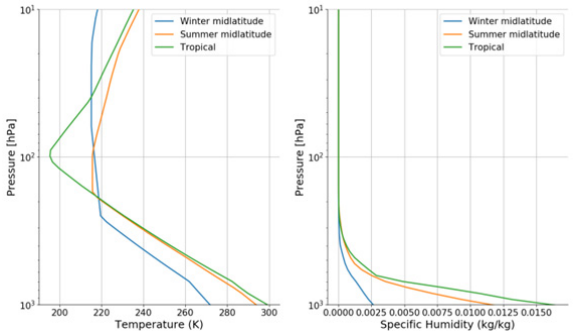

Figure 1. Atmospheric temperature and specific humidity profiles for three profiles

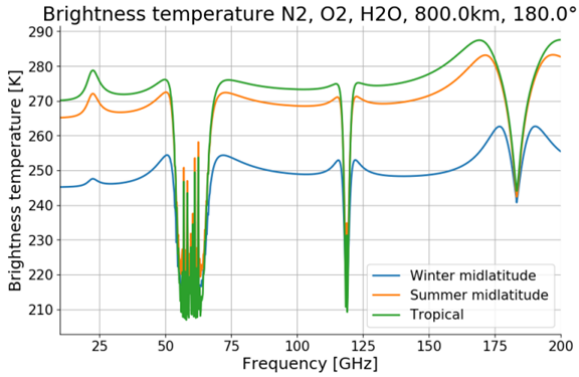

Figure 2. Brightness temperature over 10-200 GHz for three atmospheric profiles of figure 1 computed using the software ARTS [6].

SAPHIR instrument aboard Megha-Tropiques satellite launched in 2011 measures the H2O absorption band using six analog channels (double side band) at 183 GHz as shown in *Figure 3*.
For SAPHIR-NG, a new architecture with hundreds of channels is considered to improve the quality of the measurements.

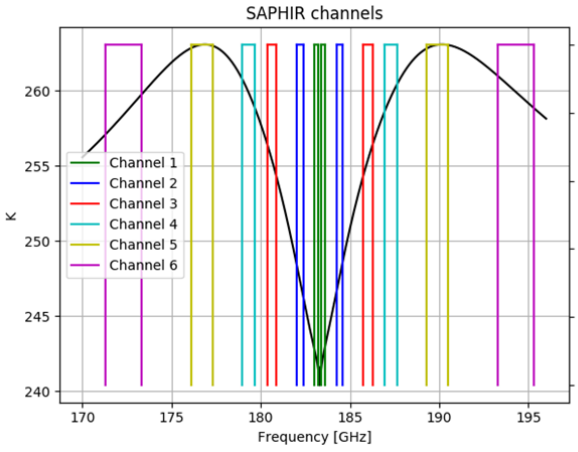

Figure 3. SAPHIR Brightness measurement channels

1.1. Radiometric Measurement principle

The power measurement made in a radiometric channel with a channel impulse response $h^i(t)$ is resulting from the filtering followed by the squaring and accumulation of the input noise:

$$T_m^i(t) = \left(n(t) * h^i(t)\right)^2 * h_{int}(t) \tag{1}$$

The noise signal *n(t)* is the addition of the natural noise collected by the antenna with a power spectral density related to the brightness temperature $T_b(f)$ of the medium and the noise created by the receiver of power spectral density $T_r(f)$. The accumulation of the power value is made using a low pass filter of impulse response $h_{int}(t)$.

The moments of the output of the channels can be computed using the wide sense stationarity of the signals (to use Wiener-Lee relations) and the Gaussian nature of the noise (to use Isserli's theorem)

In this respect the expectation and the variance of the measured power can be expressed as:

$$E[T_m^i(t)] = \left(\int |H(f)|^2 \frac{(T_b(f) + T_r(f))}{2} df\right) H_{int}(0) \tag{2}$$

$$Var[T_m^i(t)] = \left(\int |H_{int}(f)|^2 \left[4\left(|H^i(f)|^2 \frac{(T_b(f) + T_r(f))}{2}\right) * \left(|H^i(f)|^2 \frac{(T_b(f) + T_r(f))}{2}\right)\right] df\right) \tag{3}$$

If the output of another channel is considered the covariance of the measurements is given by:

$$Cov\left[T_m^i(t), T_m^j(t)\right] = \left(\int |H_{int}(f)|^2 \left[4\left(|H^i(f)|^2 \frac{(T_b(f) + T_r(f))}{2}\right) * \left(|H^j(f)|^2 \frac{(T_b(f) + T_r(f))}{2}\right)\right] df\right) \tag{4}$$

As can be seen in Eq. (2), (3) and (4), the statistical properties of the measurement depend on the characteristics of the various filters. In particular the channel width has a strong impact on the ability to discriminate small fluctuations in the power spectral density of the concatenated noise : natural + receiver noise.

Eq. (4) shows that the overlapping of channels in frequency induces a correlation of the different measurements that will introduce some redundant information that is not useful in terms of data content.

Ideally, the frequency response of the channel is a rectangular frequency window of width B and the accumulation filter is a moving average filter over a duration T as the idea is to average the information for a duration T>>1/B.

In those conditions:

$$\mathrm{E}[\mathrm{T}_{\mathrm{m}}^{\mathrm{i}}(\mathrm{t})] = \frac{1}{\mathrm{B}}\int_{\left[\mathrm{f}_{\mathrm{c}}^{\mathrm{i}}-\frac{\mathrm{B}}{2},\mathrm{f}_{\mathrm{c}}^{\mathrm{i}}+\frac{\mathrm{B}}{2}\right]} \mathrm{T}_{\mathrm{b}}(\mathrm{f}) + \mathrm{T}_{\mathrm{r}}(\mathrm{f})\mathrm{df} \qquad (5)$$

Where $\mathrm{E}[\mathrm{T}_{\mathrm{m}}^{\mathrm{i}}(\mathrm{t})]$ is the average of the noise PSD and the variance of the measurements is given by:

$$Var[T_m^i(t)] = \frac{1}{B^2T}\int_{\left[f_c^i-\frac{B}{2},f_c^i+\frac{B}{2}\right]} \left(T_b(f)+T_r(f)\right)^2 df \qquad (6)$$

Assuming a spectral flatness of the noise, those expressions becomes respectively

$$\mathrm{E}[T_m^i(t)] = T_b + T_r \qquad (7)$$

And:

$$\mathrm{Var}[T_m^i(t)] = \frac{(T_b+T_r)^2}{BT} \qquad (8)$$

Eq. (7) and (8) are the usual radiometric accuracy performance criterions with a variance of estimation that is inversely proportional to the bandwidth and to the integration time.

1.2. Receiving Chain model and calibration

The antenna and receiving chain up to the ADC can be modelled with a gain G and a flat equivalent Noise Temperature of T_{rec}. Those values are assumed independent of the frequency in a first order approximation.
The input signal is modelled as a pink Gaussian noise with power spectral density of $T_b(f)$.
The power spectral density at the input of the ADC is

$$P_{adc}(f) = G * (T_b(f) + T_{rec}) \qquad (9)$$

The hyper-spectral back-end splits this P_{adc} signal in L channels and estimates the power in each channel.
The gain G and the noise temperature T_{rec} are unknown (due to electronic fluctuation in electronic components during the equipment lifetime, temperature variations and short term instabilities).

This model is shown in Figure 4.

Figure 4. Model of the signal at input of the spectrometer

A two points calibration is performed using a cold source (usually the cosmic background) and a hot source (via a metrology noise source). The measured spectrum is shown in Figure 5.

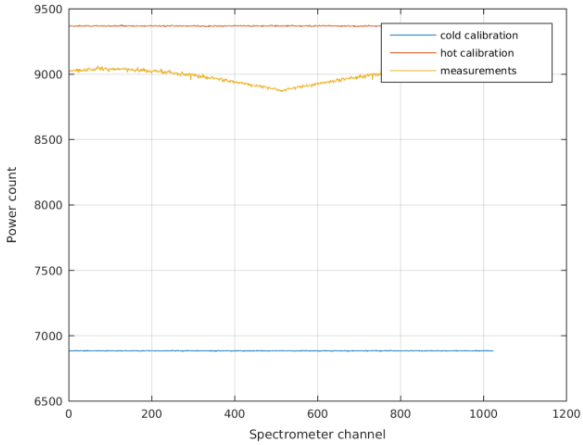

Figure 5. Simulated measurement of signal with hot and cold calibration.

From the power measurement in every channel named P, the noise temperature in the frequency band of each channel can be estimated by the linear regression in Eq. 10.

$$T = T_{cold} + \left(\frac{P-P_{cold}}{P_{hot}-P_{cold}}\right)(T_{hot}-T_{cold}) \qquad (10)$$

The result of the linear regression is presented in Figure 6.

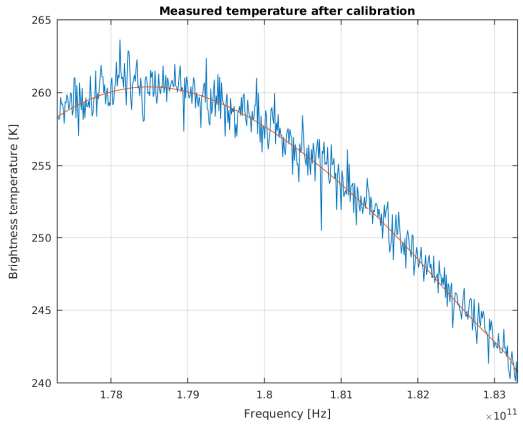

Figure 6: Measured brightness temperature (blue) and the input brightness temperature (red).

2. Impact of quantization and filtering

2.1. Information content in the frame of a polyphase filter bank with critical sampling

A widespread methodology to assess the value of measurements for inverse problems, is to measure the information content brought by the measurements ([2],[3],[4],[5]).

The general idea behind this methodology is to assess in which extent the measures decrease the uncertainty on the atmospheric state, knowing the measurements. One of the drawbacks is that this methodology is suitable only for Gaussian and small fluctuations.

In the present case the measurements to be exploited are indirect measurements of the brightness temperature of the atmosphere obtained through the transfer function of the instrument that is used to infer properties on the state of the atmosphere at various pressure or altitude levels.

The brightness temperature is linked to the atmospheric profile through the radiative transfer equation

$$T_b(\mathrm{f}) = F(f, T(p_i)_{i=1..N}, q(p_i)_{i=1..N}) \tag{11}$$

Where

- f is the frequency
- $T(p_i)$ is the atmospheric temperature at pressure $\mathrm{p_i}$
- $q(p_i)$ is the specific humidity at pressure p_i.

It can be used to establish the forward model of the measurements.

For illustrative purposes a non scattering atmosphere is considered, neglecting the impact of trace gases without significant absorption line in the mm wave range (O_3, CO_2…). The scattering case is usually much more complex to exploit with radiometric measurements. This is due to the much larger dimensionality of the radiative transfer problem that depends on the granulometric profiles of the various hydrometeor species not only in the sounded atmospheric column but also in the surrounding medium) with a strongly non linear dependence.

The key behind the information content analysis is to evaluate the difference of entropy computed on the covariance matrix of the a priori atmospheric state and the covariance matrix of the atmospheric state knowing the measurements performed by the sensor.

This covariance matrix of the atmospheric state after the measurements can be obtained from the knowledge of the a priori covariance matrix, the characteristics of the radiative transfer around the a priori state and the error characteristics of the instrument through:

$$\mathrm{S}^{-1} = \mathrm{J}^{\mathrm{T}}(\mathrm{S}_\varepsilon + \mathrm{S}_\mathrm{F})^{-1}\mathrm{J} + \mathrm{S}_\mathrm{a}^{-1} \tag{12}$$

Where :

- J is the Jacobian of the instrument around the a priori state
- S_ε is the covariance matrix of the measurements error
- S_a is the covariance matrix of the a priori error
- S_F is the covariance matrix of the error of the radiative transfer and of the transfer function of the instrument

The measurement of channel k can be modelled function of the atmospheric parameters on the $\mathrm{N_{lev}}$ pressure levels of interest by:

$$M^k(\mathrm{T(p_i)}, \mathrm{q(p_i)}) = \left(\int |H^k(\mathrm{f})|^2 \frac{(F(f, T(p_i), q(p_i)) + \mathrm{T_r(f)})}{2} \mathrm{df}\right) \mathrm{H_{int}}(0) \tag{13}$$

The terms of the Jacobian of the measurements are given by:

$$J_{ki} = \frac{\partial M^k}{\partial T_i}, J_{k(i+Nlev)} = \frac{\partial M^k}{\partial q_i} \tag{14}$$

The Shannon information can then be defined by

$$\begin{aligned} H &= S(S'_a) - S(S') \\ &= \sum_{\mathrm{i}} \frac{1}{2} \log(1 + \lambda_i^2) \end{aligned} \tag{15}$$

, where λ_i are the diagonal values from the SVD (Singular Value Decomposition) of the inverse problem renormalized by the weights of the errors (a priori and measures).

$$S_\epsilon^{-\frac{1}{2}} J S_a^{\frac{1}{2}} = U \Lambda V^T \tag{16}$$

The Shannon information can be seen as the natural logarithm of the ratio between the confidence volume of the a priori information and the volume of the confidence volume after taking into account the measurements performed by the instrument.

It is thus a convenient way to evaluate the potential usefulness of a given instrument without any assumptions on the further usage of the measurements.

It is important to keep in mind that this analysis is subject to various assumptions especially of small and Gaussian deviations of the various quantities around the a priori.

To evaluate the impact of the different filterbank parameters, a method based on information content has been used. The information content in the measured power at the output of the filterbank is analysed, for different number of channels and relative bandwidth of the channels.

In the specific frame of a polyphase filter bank, the output signal is by construction decimated by a ratio equals to the number of channels. If at the output of a filter the sampling frequency (complex) is lower than the bandwidth of the filter, the digital signal is undersampled and aliasing occurs. The power estimation variance is impacted (by a factor of B/fs) for B > fs approximately.

Table 1. Information content versus Filterbank size and filter relative bandwidth.

	Bandwidth of a channel / sample rate (complex)					
Number of channels	0.1	0.5	1	1.5	2	4
8	2.14	2.44	**2.73**	2.63	2.42	1.76
16	2.26	2.74	**3.15**	2.80	2.54	1.84
32	2.22	2.88	**3.45**	2.98	2.69	1.93
64	2.09	2.90	**3.63**	3.15	2.86	2.05
128	1.99	2.91	**3.75**	3.28	2.99	2.14
256	1.99	2.93	**3.84**	3.36	3.07	2.19
512	2.05	2.92	**3.92**	3.41	3.11	2.22
1024	2.09	3.04	**3.98**	3.44	3.12	2.23

The best channel bandwidth based on information content is when the channel bandwidth is equal to the channel spacing.

For a number of channels larger than 256 channels, the information content gain is very limited and comes to saturation.

2.2. ADC quantization

Very high speed ADC (>> 10Gsps) are based on flash ADC architecture, with a limited number of bits (3 to 5). ADC with lower sampling rate can be found with 8 to 12 bits.
The ADC transfer function changes the probability distribution of the input signal, supposed as AWGN (Additivie White Gaussian Noise) of power *var(G)* for this analysis. This will create a power measurement biases, with impact depending on input power back off and number of bits of the ADC.

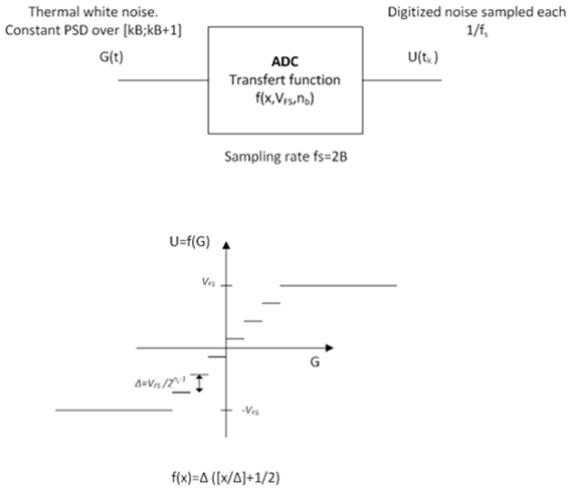

Figure 7. Model of an ideal ADC

Figure 8 shows that a range of input power exists where the quantized output power is very close to the input power. This range is greater for ADC with more quantization bits. For high level input signals, the input signal is clipped to the maximum ADC codes, leading to reduced measured power.

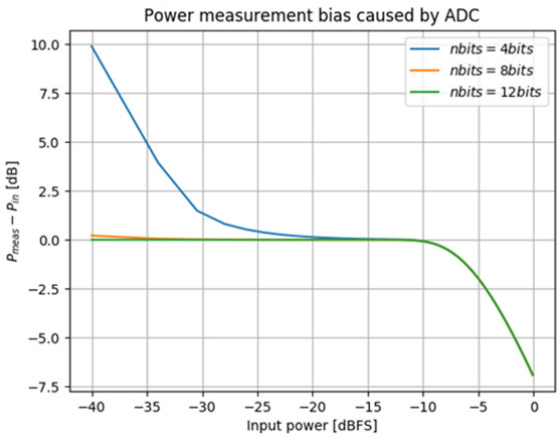

Figure 8. Power measurement bias between the input signal and the quantized output signal for an ideal ADC with different number of bits and different input AWGN power levels.

For low level input signal, the signal is impacted by the quantization step. For the ideal ADC model where the 0V level corresponds to a code transition, the quantized signal power is higher than the input signal power. Real ADC levels have an input bias, so 0 V will not

correspond to a code transition and the ADC response may be different for low level signals.

The radiometer operates by measuring the relative power of the signal measured versus the power measured for the cold source and hot source calibration signals. The impact of the ADC quantization on this radiometric bias has been evaluated for different back off and quantization bits in Tab. 2.

Table 2. Bias of radiometric temperature (K) due to ADC quantization for a linear regression between 500K and 2000K. Estimation standard deviation of 0.04K (at 1000 K).

	-0.0 dBFS	-6.0 dBFS	-9.5 dBFS	-12.0 dBFS	-14.0 dBFS	-15.6 dBFS
2 bits	293	132	-116	-367	-548	-653
3 bits	260	92	11.5	-7.37	-49	-137
4 bits	246	74	7.67	0.22	-0.03	-0.22
6 bits	232	60	5.10	0.09	-0.04	-0.05
8 bits	229	58	4.58	0.07	-0.05	-0.05
10 bits	229	57	4.46	0.06	-0.05	-0.05
12 bits	229	57	4.43	0.06	-0.05	-0.05

3. Filter bank implementation

3.1. FIR Filters

The direct method to implement a bank of digital filters is to use a bank of independent FIR filters. The input signal is filtered by *L* FIR filters operating at the sampling frequency of the ADC *fs* as illustrated Figure 9.

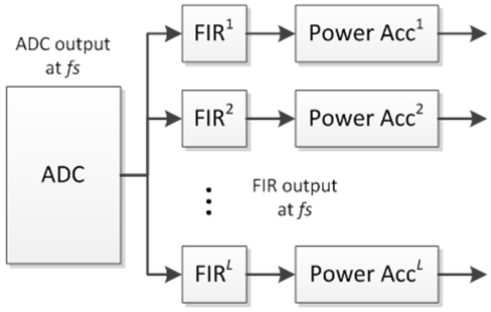

Figure 9: Bank of FIR filters for a digital spectrometer

The processing by a bank of filter is very computationally expensive. Each input sample will be multiplied by the *M* coefficients of all the *L* FIR Filters. So for each input sample, *ML* multiplications are required.

3.2. Polyphase Filter bank

The polyphase filter bank is a computationally efficient solution to implement a filterbank. It has some restrictions compared to a bank of FIR filters:

- All the filters for all the channels have the same response
- The output for each channel is decimated by *L*.
- The channels are frequency spaced by *fs/L*

By using a FFT and prefilters, the polyphase filterbank simultaneously filters *L* channels in parallel, spaced by *fs/L*.

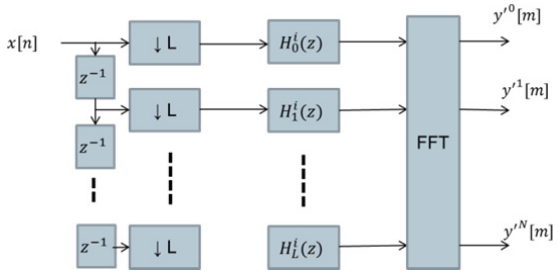

Figure 10: Polyphase filterbank to implement L filters spaced by fs/L

This structure is very efficient. To filter *L* points in *L* channels with a prototype filter of length *M,* the number of multiplications required is of the order of $M+2*L*\log2(L)$ assuming a radix 2 FFT.
(to compare to the ML^2 equivalent multiplications for a bank of FIR filters.)

An important note is that if the input signal is real, the output spectrum is symmetric, so only half of the output channels are useful.
This can be compensated by doubling the size of the FFT compared to the required channel number. Additional mathematical tricks can then be used to compute two real *L* points FFT in parallel using this complex 2*L* points FFT, by stuffing one of the input signal in the real part of the input, and the other in the imaginary part. Some additions and subtractions at the output of the FFT are used to recover the two *L* channels outputs.
A detailed derivation of the polyphase filter implementation can be found in [1].

3.3. Processing efficiency

Table 3: computation complexity for a bank of FIR filters and a polyphase filterbank.

	FIR Filters in parallel	Polyphase Filterbank
#Channels	*L*	*L*

#filter coefficients	*M*	*M*
#multiplications for *L* point inputs	*LLM*	*M*+2*L**log2(*L*)
#multiplications per input sample	*LM*	*M*/*L*+2log2(*L*)
***L*=256, *M*=768**	197k mult/sample	19 mult/sample

The polyphase filterbank shows a large efficiency gain compared to the standard FIR implementation for our application with a large number of channels.

3.4. Filter Window

Hamming Window

The frequency response of a polyphase filterbank with hamming prototype filter has been generated for a bandwidth of 6 GHz. An FFT of 1024 points has been used, see *Figure 11*.
This FFT size is optimized for Radix-4 implementation and larger than 2 times the 256 channels identified as the threshold for maximization of information content.

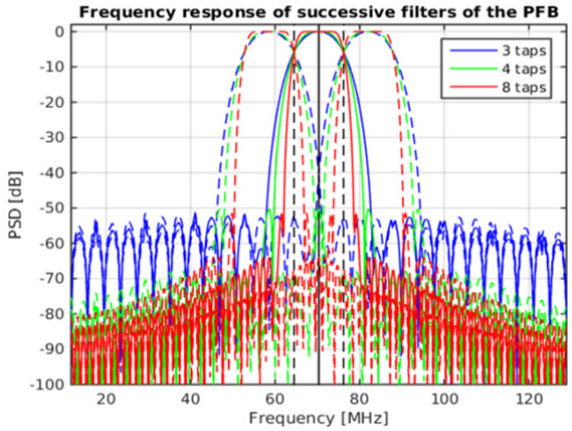

Figure 11: Response for a polyphase filterbank with 1024 complex channels (with 3 adjacent channels shown) with different number of coefficients for the prototype filter (here M tapsx1024) for a Hamming window.

Different performance metrics are shown in table 4:
- The ratio between the power of the filtered signal by a channel in the filterbank and the power of the signal filtered by and ideal brickwall filter.
- The fraction of the filtered signal power included in the equivalent brickwall filter and the two adjacent identical filters.

Blackman Harris Window

A Blackman Harris filter prototype gives the frequency response in *Figure 12*.

Table 4: Performance metrics of the polyphase filterbank for a Hamming|Blackman Harris window with different number of coefficients for the prototype filter (here M tapsx1024)

	M = 1 taps	**M = 3 taps**	**M = 4 taps**	**M = 8 taps**
power in the filter/ power in ideal filter	39% |30%	77% |76%	84% |77%	90% |87%
Ratio of signal power in the equivalent ideal filter and two adjacent filters	99% |97%	100% |100%	100% |100%	100% |100%

The performance metrics show that this method of filter generation can get frequency response close to an ideal brickwall filter.

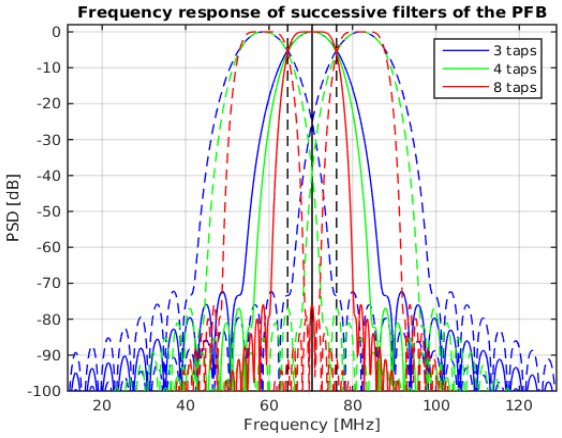

Figure 12: Response for a polyphase filterbank with 1024 complex channels (with 3 adjacent channels shown) with different number of coefficients for the prototype filter (here M tapsx1024) for a Blackman Harris window.

The Hamming filter is a bit more selective for adjacent channels, but has a lower long range selectivity, whereas Blackman Harris window is less selective for adjacent channels but has a better long range rejection.
The rejection level will be impacted for a fixed point implementation versus the levels shown here for a floating point implementation, so the high rejection of the Blackman Harris may be difficult to maintain.
A Hamming window is more interesting for a fixed point implementation of the polyphase filter bank.

4. FPGA and ADC Tradeoff

4.1. ADC

Identified discrete ADC with an equivalent spatial version are the EV12AQ600 from E2V and the TI ADC12DJ3200QML. Those two ADC allow the acquisition of up to 3.2 GHz of RF Bandwidth.

Other providers of ADC solutions in the form of hard macro IP for ASIC have been identified. Those ADC are flash based and available in radhard versions. Those hard macros can achieve power consumptions much lower than discrete ADC solutions, since a major part of the power consumption with discrete parts is linked to the data transfer between the ADC and the FPGA through high speed serial links (HSSL).

4.2. FPGA

For preliminary sizing, a resource estimation has been performed based on a polyphase filterbank with processing at 12 bits, 12.5 Gsps complex and 256 channels (complex FFT), 768 points windowing. A FPGA frequency of 195.3 MHz with a parallel ratio of 64 is used. The resources used are shown in table 5.

Table 5: Required ressources in Xilinx KU060 for the preliminary analysis

	FFT256 64 sps/clk	Power+ Accu	Polyphase FIR	others	HSSL Interface 2x 6.25Gsps
CLB LUTs	32k	8k	16k	5k	14.8k
CLB Registers	34k	8k	16k	5k	13k
DSP	432	128	384	0	0
RAM18	128	128	0	0	0
serdes	0	0	0	0	2*8@ 12.5Gbps

Table 6 show the usage for main candidate FPGAs.

Zynq Ultrascale + FPGA are interesting, but are susceptible to latch up, so not ideal for high reliability missions in space. RF-SOC version of Zynq Ultrascale+ is very interesting for the power consumption, (since the power consumption shown includes the ADC that are excluded for the other FPGAs), but it is limited by the same constraints as the standard Zynq Ultrascale+.

RTG4 FPGAs have insufficient ressources for the application.

VERSAL AI CORE are interesting FPGA, but the component maturity is currently low, and its suitability for space applications is not yet proven.

FPGA currently available with space versions are the NanoXplore NG-ultra and Xilinx KU060.

For the NG-Ultra FPGA, the 195.3 MHz frequency is not achievable with current version of the development tools, so a frequency of 97.6 MHz is used with two parallel processing instances. This leads to an overuse of the DSP ressources. Based on this preliminary result, the NG-Ultra is rejected for the breadboard demonstrator.

For the KU060, the estimated ressources are acceptable, allowing additional options in terms of quantization depth, number of channels, supported bandwidth.

Table 6: Preliminary estimate of Logic ressource use

	XQ Zynq UltraScale+ RFSoC	Space-grade Kintex UltraScale	VERSAL AI CORE	NG-Ultra
	XQ ZU28DR	XQR KU060	VC1902	NX2H540 TSC
FPGA freq. used	195.3 MHz	195.3 MHz	195.3 MHz	97.65 MHz
Power estimate	10.1 W	10.4 W	18.4 with AI Cores 17.5 only FPGA	12.1 W
RF ADC included	Yes	No	No	No
DSP use	22%	34%	48%	140%
LUT use	14%	23%	7%	42%
DFF use	7%	11%	3%	30%
BRAM use	12%	12%	13%	76%

5. Breadboard demonstrator

For the breadboard demonstrator, ADC E2V 12AQ600 will be used, based on its bandwidth and space equivalent availability. The processing will be done in a FPGA KU060, similar to the space grade version.

An evaluation board from alpha-data will be used, with a FMC mezzanine to connect with the ADC. Functional architecture of the breadboard is shown in Figure 13.

Interface (HSSL based) between the ADC and the FPGA is based on the ESISTREAM protocol used by the E2V ADC.

The data from the ADC quantization are processed by the spectrometer module. Accumulations at the output of the spectrometer are transmitted to a computer.

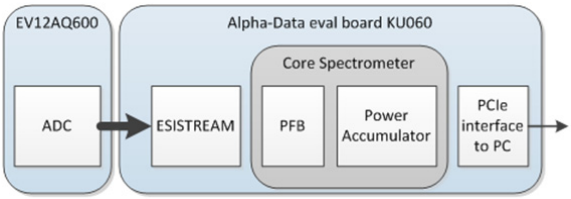

*Figure **13**: Functional architecture of the breadboard.*

ACKNOWLEDGEMENTS

This study has been performed in the frame of the CNES R&T Study : “R&T R-S20-OT-0002-101 – Maquettage d’une chaine de réception numérique pour radiomètres hyperspectraux. Application à la raie H2O à 183 GHz pour SAPHIR-NG”

REFERENCESS

[1] Price D. C. , Spectrometers and Polyphase Filterbanks in Radio Astronomy, 2016. arXiv 1607.03579.

[2] Rodgers, C. D. Information content and optimisation of high spectral resolution remote measurements, Advances in Space Research, 10.1016/S0273-1177(97)00915-0, 21, 3, (361-367),

[3] Rodgers, C. D. (2000), Inverse methods for atmospheric sounding—Theory and practice, Ser. on Atmos. Oceanic and Planet. Phys.,World Sci.,Singapore, doi:10.1142/9789812813718.

[4] Aires, F., Prigent, C., Orlandi, E., Milz, M., Eriksson, P., Crewell, S., Lin, C.-C., and Kangas, V. (2015), Microwave hyperspectral measurements for temperature and humidity atmospheric profiling from satellite: The clear-sky case, J. Geophys. Res. Atmos., 120, 11,334–11,351, doi:10.1002/2015JD023331.

[5] Mahfouf, J.-F., C. Birman, F. Aires, C. Prigent, E. Orlandi, and M. Milz (2015), Information content on temperature and water vapour from a hyper-spectral microwave sensor, Q. J. R. Meteorol. Soc., doi:10.1002/qj.2608.

[6] Buehler, S. A., J. Mendrok, P. Eriksson, A. Perrin, R. Larsson, and O. Lemke (2018), ARTS, the atmospheric radiative transfer simulator — version 2.2, the planetary toolbox edition, Geosci. Model Dev., *11*(4), 1537–1556, doi:10.5194/gmd-11-1537-2018.